Atmos. Chem. Phys. Discuss., 15, 30043–30079, 2015
www.atmos-chem-phys-discuss.net/15/30043/2015/
doi:10.5194/acpd-15-30043-2015

Atmospheric Chemistry and Physics Discussions

Climatic impacts of stratospheric geoengineering with sulfate, black carbon and titania injection

A. C. Jones[1], **J. M. Haywood**[1,2], **and A. Jones**[2]

[1]College of Engineering Maths and Physical Sciences, University of Exeter, Exeter, UK
[2]Met Office Hadley Centre, Exeter, UK

Received: 12 October 2015 – Accepted: 13 October 2015 – Published: 3 November 2015

Correspondence to: A. C. Jones (aj247@exeter.ac.uk)

Published by Copernicus Publications on behalf of the European Geosciences Union.

Abstract

In this paper, we examine the potential climatic effects of geoengineering by sulfate, black carbon and titania injection against a baseline RCP8.5 scenario. We use the HadGEM2-CCS model to simulate scenarios in which the top-of-the-atmosphere radiative imbalance due to rising greenhouse gas concentrations is offset by sufficient aerosol injection throughout the 2020–2100 period. We find that the global-mean temperature is effectively maintained at historical levels for the entirety of the period for all 3 aerosol-injection scenarios, though there are a wide range of side-effects which are discussed in detail. The most prominent conclusion is that although the BC injection rate necessary to produce an equivalent global mean temperature-response is much lower, the severity of stratospheric temperature changes (> +70 °C) and precipitation impacts effectively exclude BC from being a viable option for geoengineering. Additionally, while it has been suggested that titania would be an effective particle because of its high scattering efficiency, it also efficiently absorbs solar ultraviolet radiation producing a significant stratospheric warming (> +20 °C). As injection rates for titania are close to those for sulfate, there appears little benefit of using titania when compared to injection of sulfur dioxide, which has the added benefit of being well modelled through extensive research that has been carried out on naturally occurring explosive volcanic eruptions.

1 Introduction

The climatic impacts of continued greenhouse gas (GHG) emissions are likely to be severe which has prompted countenance of new strategies for tackling GHG-induced global warming (e.g Collins et al., 2014). Geoengineering strategies, or large-scale climate interventions that aim to reduce global warming, include strategies to sequester atmospheric carbon dioxide – Carbon Dioxide Removal (CDR) methods, and strategies to reduce solar irradiance at Earth's surface – Solar Radiation Manage-

ACPD
15, 30043–30079, 2015

ment (SRM) methods (Shepherd et al., 2009). Stratospheric Aerosol Injection (SAI), an SRM scheme which has received significant attention, involves the enhancement of the stratospheric aerosol layer in order to reflect more sunlight back to space. This scheme mimics large volcanic eruptions such as Mt. Pinatubo in 1991, which injected approximately 15–20 Tg of sulfur dioxide (SO_2) into the tropical stratosphere and induced a globally averaged surface cooling of around −0.3 °C for the following two years (Stenchikov et al., 2002).

Sulfate (SO_4) aerosols have featured predominantly in SAI research because of the volcanic analogue (e.g. in the Geoengineering Model Intercomparison Project, GeoMIP, Kravitz et al., 2013). General Circulation Model (GCM) simulations suggest that, while sufficient sulfate injection could effectively reduce global-mean temperature, possible side effects include changes to regional precipitation (e.g. Bala et al., 2008; Tilmes et al., 2013), ozone (e.g. Tilmes et al., 2009; Pitari et al., 2014), stratospheric dynamics (Aquila et al., 2014) and sea-ice extent (Berdahl et al., 2014). Precipitation changes could result from changes to the moist static stability of the atmosphere and a concomitant weakening of the hydrological cycle (Bala et al., 2008), and the regional precipitation changes under GeoMIP simulations have been shown to be reasonably consistent across a range of climate models (Tilmes et al., 2013). Ozone concentrations could change as a result of enhanced heterogeneous chemistry on the surface of sulfate aerosols or indirectly by changes to the stratospheric dynamics and chemistry (e.g. Tilmes et al., 2009). Stratospheric dynamical changes could occur as the result of tropical heating in the sulfate layer and by changes to wave propagation from the troposphere (e.g. Aquila et al., 2014).

In order to ameliorate the known side-effects of sulfate injection, some authors have proposed alternative aerosols to sulfate (e.g. Teller et al., 1997). Crutzen (2006) suggested the possible injection of black carbon (BC), which would mimic hypothetical nuclear winter scenarios. One advantage of BC over sulfate is that less mass would be needed for an equivalent radiative forcing (Crutzen, 2006). BC particles efficiently absorb solar radiation, unlike sulfate which primarily reflects solar radiation (Ferraro

ACPD
15, 30043–30079, 2015

et al., 2011). Alternatively, minerals such as titania (TiO_2), silica (SiO_2) and alumina (Al_2O_3), which have a high refractive index at wavelengths of peak solar radiative flux (~ 550 nm), have also been suggested (Pope et al., 2012). Although the use of alternative aerosols is not a new suggestion (e.g. Teller et al., 1997), comparatively little research has been conducted on their potential utility. Kravitz et al. (2012) simulated a constant BC injection scenario of 1 Tg yr^{-1} in the tropics for small radius (0.03 µm) and large radius (0.15 µm) aerosols. They found that the small particle BC aerosol scenario produced a global surface cooling of −9.45 °C, but also induced stratospheric warming > +60 °C and global ozone loss of 50 %. The large particle BC aerosol scenario had a neglible climatic impact. Using a fixed dynamical heating (FDH) code, Ferraro et al. (2011) compared the stratospheric heating of sulfate, titania, and BC layers for an equivalent instantaneous radiative forcing. Their results showed a tropical stratospheric warming signal for all the aerosols, though much greater in the case of BC. To date, no work has used a comprehensive fully coupled atmosphere–ocean GCM to directly compare the possible climatic impacts of SAI with alternative aerosols to sulfate, which is the motivation for this research.

In this work, we simulate the stratospheric injection of sulfate, titania and BC against a baseline RCP8.5 concentrations scenario using a fully-coupled GCM. Titania is selected to represent an efficient light-scattering aerosol and BC is selected as a light-absorbing aerosol. RCP8.5 is selected to give a significant greenhouse effect against which to employ geoengineering, in order to distinguish the climatic impacts specific to each aerosol. We chose to inject aerosol at a sufficient rate to counterbalance the Top Of the Atmosphere (TOA) global/annual-mean Radiative Flux (TOA-RF) imbalance caused by increasing atmospheric GHGs. Our simulation design is similar to the G3 scenario of the Geoengineering Model Intercomparison Project (GeoMIP), which instead used the RCP4.5 concentrations scenario as its baseline and injected sulfate at a sufficient rate to counterbalance GHG radiative forcing (Kravitz et al., 2011). We analyse the climate changes in the 2090s with respect to a simulated historical period and discuss impacts on a wide range of meteorological parameters.

ACPD
15, 30043–30079, 2015

2 Model

2.1 The HadGEM2-CCS model

For this investigation, we use the HadGEM2-CCS climate model in a fully coupled atmosphere–ocean mode. HadGEM2-CCS is the high-top configuration of the HadGEM2 family of models, and includes a well-resolved stratosphere. The atmosphere component comprises 60 vertical levels extending to 84 km and a horizontal resolution of 1.25° × 1.875° latitude by longitude respectively. The 40-level ocean component has a horizontal resolution of 1° by 1° from the poles to 30° N/S, with the latitudinal resolution then increasing smoothly to 0.33° at the equator (The HadGEM2 Development Team, 2011). For this investigation, GHG concentrations, stratospheric ozone, anthropogenic aerosols and aerosol precursor gases are prescribed following the Coupled Model Intercomparison Project phase 5 (CMIP5) (Taylor et al., 2012) protocol, with historical data from 1860–2005 and RCP8.5 concentrations from 2005–2100. HadGEM2-CCS contains the aerosol module Coupled Large-scale Aerosol Simulator for Studies in Climate (CLASSIC). The module's sulfur cycle is described in detail in Bellouin et al. (2011). Briefly, it includes the oxidation of sulfur dioxide (SO_2) to sulfate aerosol in aqueous and gas phase reactions. Sulfate is represented by Aitken, accumulation and dissolved modes, with hygroscopic growth in the accumulation mode following d'Almeida et al. (1991). Aerosol size modes are represented by lognormal size-distributions with a prescribed dry-mode median radius (r_m) and geometric standard deviation (σ).

2.2 Stratospheric aerosol microphysical and optical properties

For this investigation, stratospheric sulfate is modelled using the *volc2* size-distribution from Rasch et al. (2008) for the sulfate accumulation mode, with $r_m = 0.376\,\mu m$ and $\sigma = 1.25$; the relatively large r_m is chosen to reflect the high concentrations of SO_2

ACPD
15, 30043–30079, 2015

injected in this experiment. Hygroscopic growth is parameterised following Deepak and Gerber (1983).

CLASSIC includes a tropospheric BC scheme with fresh, aged and in-cloud modes (Bellouin et al., 2011). We introduce an additional non-hygroscopic stratospheric BC component and prescribe a lognormal size-distribution with $r_m = 0.0118\,\mu m$ and $\sigma = 2.0$, which is taken from tropospheric BC observations (Deepak and Gerber, 1983). We prescribe a density for BC of $1000\,kg\,m^{-3}$ and take refractive indices from a World Meteorological Organisation report (Deepak and Gerber, 1983).

For stratospheric titania, we assume the non-hygroscopic lognormal size distribution of Pope et al. (2012) with $r_m = 0.045\,\mu m$ and $\sigma = 1.8$. This size-distribution was selected to give the titania aerosol a high scattering efficiency, as shown by Pope et al. (2012). We prescribe a density for titania of $4230\,kg\,m^{-3}$ (Pope et al., 2012), and for the refractive indices we follow Ferraro et al. (2011) and use the average of the extra-ordinary and ordinary values from Ribarsky (1984).

The specific absorption (k_{abs}) and scattering (k_{sca}) coefficients for sulfate (accumulation/dry-mode), titania and BC are plotted in Fig. 1 as a function of wavelength. For sulfate, the specific extinction coefficient (k_{ext}) at 500 nm of $3200\,kg\,m^{-3}$ and single scattering albedo (ω_o) of 1 reflects the non-absorbing properties of sulfate. Although titania's 500 nm scattering efficiency ($k_{sca} = 3850\,kg\,m^{-3}$) is greater than sulfate's in this instance, titania additionally absorbs SW radiation ($k_{abs} = 2000\,kg\,m^{-3}$ at 250 nm, and $k_{abs} = 600\,kg\,m^{-3}$ at 500 nm) which can be explained by the band-theory of solids (Yang et al., 2003). Thus titania is partially absorbing. Our modelled BC efficiently absorbs SW radiation ($k_{abs} = 8300\,kg\,m^{-3}$ at 500 nm) but also produces a non-negligible SW scattering effect ($k_{sca} = 2500\,kg\,m^{-3}$ at 500 nm) which is comparable in magnitude to the equivalent scattering efficiency of both titania and sulfate. Therefore, to describe titania as an efficient light-scatterer and/or BC as an efficient light-absorber is an over-simplification.

Our choice of particle size and density will impact the aerosol's gravitational sedimentation rate and therefore its atmospheric residence time (the sedimentation rate is

ACPD
15, 30043–30079, 2015

also a property of the local atmospheric conditions) (Rasch et al., 2008). To determine the importance of our choice of aerosol properties, we have calculated the respective gravitational sedimentation rates by using the method of Pruppacher and Klett (1979) (which utilises Stoke's law) and incorporating temperature and pressure values from the International Standard Atmosphere (ICAO, 1993) (Fig. S1 in the Supplement). We find that the average sedimentation rates between 18–26 km altitude for our prescribed sulfate, titania, and BC are 23, 9.5 and 0.75 m day^{-1} respectively, and the equivalent rates between 26–30 km are 52, 22, and 1.8 m day^{-1}. Therefore, one would expect BC to be advected to much higher altitudes than sulfate in these simulations. For perspective, Schoeberl et al. (2008) deduced from observations that the atmospheric tropical vertical velocity between 18–26 km has an upper limit of 35 m day^{-1}, and the equivalent velocity between 26–30 km is below 61 m day^{-1}.

3 Method

We first validated the model's stratospheric sulfate scheme by simulating the Mt. Pinatubo eruption and then comparing the results with observations. These simulations comprised a 10-member ensemble in which 20 Tg SO_2 is injected between 16–18 km over a single day in June 1991, following the method of Aquila et al. (2012). Figure 2a shows the global/annual-mean sulfate aerosol optical depth (AOD) anomaly for the HadGEM2-ensemble and for AVHRR and SAGE-II observations. The model clearly captures the peak AOD from the AVHRR data, and the exponential decline thereafter. Figure 2b–d shows the zonal-mean AOD anomaly for the same time period. The agreement between the model and observed AOD is reasonable. Some differences in the temporal evolution of the AODs in the model and the observations are due to the almost concurrent eruption of Cerro Hudson which injected approximately 3.3 Tg SO_2 into the Southern Hemisphere (Deshler and Anderson-Sprecher, 2006). This relatively close agreement between observations and HadGEM2 estimates, together with other

ACPD
15, 30043–30079, 2015

modelling studies of other volcanic eruptions (Haywood et al., 2010) suggests that the model is a useful tool for stratospheric geoengineering simulations.

The geoengineering investigation was based on a 240 year Pre-Industrial Control simulation (forced by constant 1860's GHGs and aerosol emissions) and historical simulations for the period 1860–2005 following CMIP5 (Taylor et al., 2012) protocol followed by RCP8.5 emission specified from 2005–2019. Leading on from these simulations, we performed 3-member ensembles for the period 2020–2100 for: RCP8.5 only, RCP8.5 with SO_2 injection (G3S), RCP8.5 with TiO_2 injection ($G3TiO_2$), and RCP8.5 with BC injection (G3BC). The G3 nomenclature is adopted because of the similarity of our simulations to the G3 experiments of GeoMIP although the original G3 experiments were compared against RCP4.5 and the geoengineering period was terminated at 2070 (Kravitz et al., 2011). Aerosol (or gaseous SO_2 for the G3S scenario) was injected at a constant rate between 23–28 km altitude in a single vertical column at the equator. The injection altitude and location were chosen to prolong the stratospheric lifetime of the aerosol, which is transported poleward by the upper branch of the Brewer–Dobson circulation (Niemeier et al., 2011), and therefore make the geoengineering approach reasonably efficient. To determine the injection rates required to maintain TOA-RF balance, we first conducted 10 year atmosphere-only simulations of 1 Tg aerosol (or SO_2 for sulfate) injection per year to calculate the specific radiative effect for each aerosol. We then used the radiative effect to calculate the injection rate necessary to offset the RCP8.5 anthropogenic radiative forcing (ARF) for the 2020–2100 period (with ARF values from Meinshausen et al., 2011). As the geoengineering simulations progressed, we altered the injection rate when necessary to ensure that TOA-RF balance was maintained.

Our analysis focuses initially on the temporal evolution of the TOA-RF and global mean temperature changes to show that our simulations provide plausible counterbalances to global mean temperature changes under RCP8.5. However, our main focus is on the differences between the recent historical period (1980–2005) (hereafter de-

ACPD
15, 30043–30079, 2015

noted HIST) and the geoengineering experiments during the period 2090–2100, with an emphasis on different geographical patterns.

4 Results

4.1 Effectiveness at maintaining global mean TOA-RF and near surface temperature

Figure 3 shows the global/annual-mean TOA-RF imbalance and near-surface air temperature anomaly for the geoengineering and RCP8.5 simulations, with respect to the HIST period. For all of the geoengineering simulations we were able to maintain TOA-RF balance for the entirety of the 80 year period (Fig. 3a). For G3S, G3TiO$_2$ and G3BC, the TOA-RF was maintained within ±0.21, ±0.18 and ±0.20 W m^{-2}, respectively (1 standard deviation throughout the 2020–2100 period).

However, the near-surface global temperature response differs between the aerosols with a greater cooling effect for sulfate than for titania or BC. This is due to the absorption of radiation by BC (and a lesser extent the absorption by titania) heating the stratosphere which then increases the terrestrial longwave radiation entering the troposphere reducing the tropopause-RF. As noted in several Intergovernmental Panel on Climate Change reports (e.g. Ramaswamy et al., 2001; Forster et al., 2007), it is the global mean tropopause-RF rather than the TOA-RF that is proportional to global mean surface temperature changes. Further analysis of stratospheric temperature changes will be provided in Sect. 4.4.

4.2 Aerosol distribution

The time-averaged injection rates for the 2090s period are 14 Tg SO$_2$ yr^{-1}, 5.8 and 0.81 Tg yr^{-1} for G3S, G3TiO$_2$ and G3BC, respectively. This SO$_2$ injection rate is approximately equivalent to 1 Mt. Pinatubo eruption per year (Dhomse et al., 2014).

ACPD
15, 30043–30079, 2015

These injection rates equate to global aerosol mass-burden anomalies of 49.5, 20.2, and 5.1 Tg for G3S, G3TiO_2 and G3BC, respectively. The G3BC mass burden is comparable to the equilibrium burdens of the high-altitude (HA) and small-radius (SmR) experiments from Kravitz et al. (2012), although they injected BC at a constant rate of 1 Tg yr^{-1}, around 20 % higher than in our study. Figure 4 shows the 2090s annual, June-July-August (JJA) and December-January-February (DJF) aerosol mass concentration anomalies (annual mean aerosol optical depths are shown in Fig. S2 in the Supplement). Peak sulfate concentrations are found at the injection region at the equator (Fig. 4a, d, and g) and over the winter pole. Titania and BC reach greater altitudes than sulfate (> 50 km), which is due to their smaller size-distributions and self-lofting from SW-absorption (Kravitz et al., 2012). While sulfate aerosol concentrations are highest at the equator, the highest concentrations of BC are found in the polar stratosphere. This is because the larger particle size of the sulfate aerosol is subject to a larger sedimentation velocity (see Fig. S1 in the Supplement) and thus a greater fraction of aerosol is removed close to the source region. The results from titania suggest a spatial distribution intermediate between sulfate and BC owing to the intermediate size distribution.

Figure 5 shows the total annual, JJA and DJF aerosol deposition anomalies averaged over the 2090s (the seasonal cycle of the deposition anomalies are shown in Fig. S3 in the Supplement). Sulfate is predominantly deposited in the Northern Hemisphere (NH) extratropics in the boreal spring and summer (Fig. 5d) which is likely attributable to tropopause fold events in the lower branch of the Brewer–Dobson circulation (BDC) (Kravitz et al., 2012). In contrast, Titania and BC are primarily deposited at high latitudes in the polar winter, which is attributable to the diabatic descent of air in the deep branch of the BDC (e.g. Tegtmeier et al., 2008). Kravitz et al. (2012) also found in their SmR experiment that BC deposition was limited to the polar regions, but their maximum deposition was during polar summer rather than polar winter. The global/annual-mean deposition rates of sulfate and BC from geoengineering are 37 and 1.5 mg m^{-2} yr^{-1}, respectively. These amounts may be compared with 231 and

ACPD
15, 30043–30079, 2015

$12.7\,mg\,m^{-2}\,yr^{-1}$ from non-geoengineering sources, amounting to increases of 16 and 12 % respectively.

4.3 Temperature and precipitation

Figure 6 shows the annual mean near-surface air temperature (Fig. 6a–d) and precipitation anomalies (Fig. 6e–h) with respect to HIST. RCP8.5 (Fig. 6a) shows the typical global warming signal of amplified warming at high-latitudes due to the positive snow-albedo feedback (e.g. Kharin et al., 2013). This results in an annual mean warming of +11.3 °C averaged over the Arctic region (> 60° N) and an average NH land warming of +7.3 °C. This figure provides an alarming picture of the change in global mean temperature by the end of this century should global society follow the RCP8.5 (essentially a business as usual) pathway. All 3 SAI experiments produce a surface-cooling with respect to RCP8.5, with G3S exhibiting the greatest global-mean cooling effect of −4.85 °C. The latitudinal distribution of cooling varies markedly between the SAI experiments, with relative tropical cooling for G3S and $G3TiO_2$ (Fig. 6b and d) and polar cooling for G3BC (Fig. 6c). Defining the "SAI cooling effect" as the temperature difference between SAI and RCP8.5, the ratio of cooling effect at high latitudes (> 60°) between G3BC and G3S is 1.19 and between G3BC and $G3TiO_2$ is 1.23. In the tropics and mid-latitudes (< 60°) the equivalent ratios are 0.64 and 0.71 respectively. The high-latitude cooling in the case of G3BC is attributable to the zonal distribution of BC (Fig. 4c, f and i) which is more evenly spread over the stratosphere than for G3S and $G3TiO_2$. The result is a greater surface SW forcing at high-latitudes in the summer hemisphere for G3BC. For instance, in the Arctic (> 60° N) in JJA, the surface SW forcing is $-25.65\,W\,m^{-2}$ in G3BC and −3.3 and $-6.55\,W\,m^{-2}$ in G3S and $G3TiO_2$ respectively.

Although the global-mean precipitation rate increases for the RCP8.5 scenario (Fig. 6e), certain regions such as the Amazon basin exhibit a drying trend. This is in line with the CMIP5 multi-model projections documented in the Intergovernmen-

ACPD
15, 30043–30079, 2015

tal Panel on Climate Change 5th assessment report (IPCC AR5) (e.g. Fig. 12.7 from Collins et al., 2013). All of the SAI experiments show a global-mean precipitation reduction with respect to both HIST and RCP8.5 (Fig. 6f–h), which is due to the deceleration of the hydrological cycle and is a robust model response to SAI (e.g. Yu et al., 2015; Tilmes et al., 2013; Bala et al., 2008). The magnitude of the precipitation changes are greater for G3BC than for G3S or $G3TiO_2$; for instance, the global mean precipitation anomaly is $-0.26\,mm\,day^{-1}$ for G3BC compared to $-0.12\,mm\,day^{-1}$ for G3S and $-0.14\,mm\,day^{-1}$ for $G3TiO_2$. This is because the stratospheric heating in G3BC applies an additional LW forcing at the tropopause and TOA which must be ameliorated by additional SW absorption in order to maintain radiative balance (Ferraro et al., 2011). The troposphere is relatively transparent to SW radiation but absorbs efficiently in the LW spectrum, therefore the annual-mean surface radiative forcing in the G3BC experiment is greater ($-10.2\,W\,m^{-2}$) than for G3S or $G3TiO_2$ (-5.1 and $-6.06\,W\,m^{-2}$ respectively – see Fig. S4 in the Supplement). Bala et al. (2008) showed that the magnitude of the precipitation response is dependent on the surface radiative imbalance; therefore the precipitation reduction is amplified in G3BC.

Figure 7 shows the JJA temperature (Fig. 7a–d) and precipitation (Fig. 7e–h) anomalies. In the G3S and $G3TiO_2$ scenarios, the temperature is effectively maintained at HIST levels (Fig. 7b and d). However, a slight bias towards high-latitude NH warming in G3S and $G3TiO_2$ results in a northward displacement of the Inter-Tropical Convergence Zone (ITCZ), which is exemplified by the Sahelian precipitation increase in Fig. 7f and h. This phenomenon was noted by Haywood et al. (2013) and has been observed after large hemispherically asymmetric volcanic eruptions (Oman et al., 2006). Although the general pattern of precipitation change is similar for the 3 SAI scenarios, G3BC again displays a greater drying signal, with 80 % of the total land area experiencing a JJA precipitation reduction in G3BC compared to 70 % for $G3TiO_2$, 57 % for G3S and 52 % for RCP8.5.

Figure 8 shows the DJF temperature (Fig. 8a–d) and precipitation (Fig. 8e–h) anomalies. The temperature reduction over Greenland in G3BC (Fig. 8c) is due to the signif-

ACPD
15, 30043–30079, 2015

icant decrease in downwelling SW radiation at the surface during the Arctic sea-ice formation season (September-October-November), which leads to a positive sea-ice albedo feedback and further localised cooling. This inference is corroborated by Fig. 9, which shows the Arctic DJF sea-ice extent in terms of the average DJF sea-ice boundary (the Antarctic DJF sea-ice extent is shown in Fig. S5 in the Supplement). The sea-ice boundary in G3BC (Fig. 9c) extends to well below Greenland, and the total sea-ice extent anomaly is +1.72 million km^2 which vastly exceeds the HIST standard deviation of ±0.52 million km^2. In comparison, the sea-ice extent anomaly of −11 million km^2 for RCP8.5 (Fig. 9a) marks a reduction by 43 % of the total HIST sea-ice extent. Returning to Fig. 8, the poleward shift in the NH extratropical rain-belt over the Atlantic in RCP8.5 (Fig. 8e) is a robust result of GHG-induced global warming and is related to storm track displacement (Lombardo et al., 2015). This same response is evident in the geoengineering simulations (Fig. 8f–h), although to a much lesser extent in G3S and G3TiO$_2$.

4.4 Stratospheric changes

Figure 10 shows the zonal-mean temperature change as a function of latitude and altitude for the JJA and DJF seasons. The stratospheric cooling in conjunction with tropospheric warming in RCP8.5 (Fig. 10a and e) is a robust result of increasing GHG-concentrations (e.g. Schmidt et al., 2013). Aerosols directly affect temperature by absorbing radiation, and indirectly by scattering radiation and by ambient dynamical and chemical changes (Carslaw and Kärcher, 2006). Sulfate predominantly absorbs in the LW and near-infrared spectrum (Fig. 1a), therefore the stratospheric radiative heating in G3S is mostly confined to the tropical region, where the stratosphere is significantly colder than the underlying warm troposphere (Ferraro et al., 2011). In contrast, titania and BC absorb in both the SW and LW spectrum (Fig. 1b and c), and therefore preferentially warm the summer-hemisphere and tropical stratosphere, where solar radiation is most prevalent. G3BC produces the most significant warming effect, with an average stratospheric (15–50 km altitude) temperature increase of +33 °C and a maximum tem-

ACPD
15, 30043–30079, 2015

perature increase of +68 °C, which occurs in JJA (Fig. 10c and g). The maximum BC-induced heating relative to the baseline RCP8.5 scenario is +76 °C (Fig. S6 in the Supplement), which is comparable to the ∼ 80 °C temperature change Kravitz et al. (2012) found in their SmR scenario. For comparison, the maximum sulfate-induced and titania-induced heating relative to RCP8.5 are far more modest at +7 and +22 °C, respectively.

A warming of the lower tropical stratosphere could have multiple climatic repercussions such as a weakening of the tropical circulation (Ferraro et al., 2014), strengthening of the polar vortex (Driscoll et al., 2012) and modification of the Quasi-Biennial Oscillation (QBO) (Aquila et al., 2014). A strengthening of the polar vortex could be instigated by an increased temperature gradient between the tropical/mid-latitude and polar stratospheres, a phenomenon which was observed after the Pinatubo eruption (Stenchikov et al., 2002). We concentrate on the Arctic wintertime (DJF) response to SAI, and adopt a similar metric to that used by Ferraro et al. (2011) to determine the stratospheric temperature gradient. Explicitly, we determine the difference in temperature between 20° N–20° S (Tropics) and 50–90° N (North Pole) at 17–22 km altitude in the DJF season. Using this metric, the change in temperature gradients for G3BC, G3S and G3TiO$_2$ are +10.4, +7, and +10.1 °C, respectively, indicating a steeper temperature gradient between the tropics and poles. Additionally, Fig. 11 shows the 50 hPa DJF geopotential height anomalies over the Arctic for RCP8.5 and the 3 SAI experiments. The negative geopotential height anomaly centered over the North Pole in all the SAI experiments is indicative of a strengthened polar night jet and a positive Arctic Oscillation phase (Stenchikov et al., 2002). The DJF zonal-mean zonal-wind anomaly (Fig. S7 in the Supplement) substantiates our inference of a strengthened polar-night jet under SAI, with increased zonal windspeeds at 65° N/40 km altitude of 62, 17, and 37 m s^{-1} for G3BC, G3S, and G3TiO$_2$ respectively.

The Quasi-Biennial Oscillation (QBO) is a periodic change in the equatorial zonal wind pattern in the stratosphere, which fluctuates between easterly and westerly-shear phases (Baldwin et al., 2001). Aquila et al. (2014) showed that radiative heating in the aerosol layer could prolong the westerly-phase of the QBO (where the phase is defined

ACPD
15, 30043–30079, 2015

at 40 hPa) by enhancing the residual-mean upwelling motion and strengthening the westerly winds. HadGEM2-CCS includes a non-orographic gravity wave scheme that permits the model to internally generate a QBO and is therefore capable of assessing QBO changes (The HadGEM2 Development Team, 2011). The average QBO period for the HIST-era ensemble is 27 months (Fig. S8 in the Supplement) which agrees closely with observations (e.g. Baldwin et al., 2001). Figure 12 shows the 2090s QBO timeseries for one ensemble member of the RCP8.5 and SAI experiments (Fig. S9a and b in the Supplement shows the QBO timeseries for the other 2 ensemble members). The average QBO periods for this timespan, which are determined using all 3-ensemble members, are 20 months for RCP8.5, 31 months for G3S and 36 months for $G3TiO_2$. For G3BC, the periodicity of the QBO extends beyond the 10 year span considered here, suggesting a persistent westerly-phase such as observed by Aquila et al. (2014) in their $G_5^{22-25\,\mathrm{km}}$ scenario. In their HadGEM2-CC simulations, Kawatani and Hamilton (2013) also observed a decline in the QBO period for the RCP8.5 scenario, although they were unable to provide a reason for this. A robust inference from this work is that the magnitude of SAI's impact on stratospheric zonal winds correlates with the magnitude of the stratospheric warming.

5 Discussion

In this work, we have assessed the climatic impacts of sulfate, black carbon and titania-injection against a baseline RCP8.5 scenario, by comparing the 2090s climate with a simulated historical period. We have shown that, although the distribution of climate changes are similar for the 3 SAI scenarios, the magnitude of the changes differ, for instance BC produces a substantially greater stratospheric warming signal with concomitantly greater changes to stratospheric dynamics. Additionally, producing an equivalent top of the atmosphere radiative perturbation with a SW-absorbing aerosol such as BC (or to a lesser extent titania) compared to a SW-scatterer such as sulfate, produces a greater SW forcing at the surface which could further disrupt the hydrological cycle

ACPD
15, 30043–30079, 2015

beyond the hydrological perturbation expected for sulfate injection. The G3BC scenario displays a greater cooling at high-latitudes than the G3S and G3TiO_2 scenarios (Figs. 6–8), which comparatively exhibit a net tropical cooling. This raises the question of whether a combination of aerosols could potentially be injected to produce a zonally-homogeneous cooling if necessary. Although SAI with sulfate and titania effectively maintains the regional distribution of temperature at HIST levels, with a slight residual warming at high latitudes, the hydrological cycle decelerates substantially in all SAI scenarios which is exemplified by a global-mean reduction in precipitation. However, annual-minimum sea-ice extent in both hemispheres and global-mean thermosteric sea-level (Fig. S10 in the Supplement) is almost entirely maintained at HIST levels for all SAI scenarios.

It is important to note that the climate impacts described above are dependent on the optical properties of the aerosol, which are further dependent on the aerosol particle's size, shape, and composition (e.g. Kravitz et al., 2012). In this investigation, the dry-mode size distribution of the aerosol species is held constant, and hygroscopic growth is not represented in the BC and titania schemes, nor are the effects of internal mixing represented. The injection of aerosol into pre-existing aerosol layers would lead to larger particles through coagulation and condensation, which further alters the aerosol's optical properties. The actual size of the aerosol in an SAI scheme would therefore depend on the injection strategy (e.g. location/season) and the size and composition of the injected species (e.g. Carslaw and Kärcher, 2006; Heckendorn et al., 2009). Recent research from Heckendorn et al. (2009), Pierce et al. (2010), English et al. (2012), and Weisenstein et al. (2015) have highlighted the importance of representing aerosol growth in SAI simulations. A detailed assessment of the aerosol microphysics for sulfate, BC, and titania injection is not within the scope of this paper, but presents an important subject for future work.

We have used prescribed ozone fields in these simulations because representing stratospheric chemistry is prohibitively computationally expensive for the multiple centennial simulations performed here (The HadGEM2 development team, 2011). Kravitz

ACPD
15, 30043–30079, 2015

et al. (2012) showed that BC injection could potentially result in global ozone depletion of $> 50\,\%$, therefore the chemistry changes in SAI could potentially exceed the importance of the physical changes in terms of climatic impacts (e.g. UV radiation at the surface). Tilmes et al. (2012) showed that SW-scattering by geoengineered sulfate could potentially compensate for ozone-loss by back-scattering UV radiation in the tropics, but that this effect was insufficiently compensatory at high latitudes. Their result was scenario-dependent; ozone loss due to heterogeneous chemistry is enhanced for smaller particles and in the presence of higher free-radical concentrations. Therefore, additional research is needed in order to understand the effects on atmospheric chemistry of injecting alternative aerosols.

Another important aspect of SAI which is comparatively under-researched is the potential for impacts on human health. Aerosol concentrations in the air near the surface are of interest because of potential human respiratory impacts (Robock, 2008). For instance, the USA's National Institute for Occupational Safety and Health (NIOSH) recommends a maximum exposure limit of $0.3\,\mathrm{mg\,m^{-3}}$ for ultrafine titania particles (Dankovic et al., 2011). In our simulations, the maximum 2090's near-surface air concentration of titania (e.g. Fig. 4) for land regions between 60° S–60° N is $254\,\mathrm{ng\,m^{-3}}$, which is of the order of 10^3 less than the NIOSH exposure limit. The equivalent maximum concentration anomalies of BC in G3BC and SO_4 in G3S are 10 and $1851\,\mathrm{ng\,m^{-3}}$ respectively. More work is needed to assess the potential impacts of SAI on air quality and human health.

Another thus far unmentioned aspect of this research is the potential for surface albedo modification by aerosol deposition. In particular, BC deposition on snow reduces the snow albedo through enhanced snow-melt and the coarsening of snow grains, which results in amplified high-latitude warming (Marks and King, 2013). HadGEM2-CCS does not include the BC-on-snow feedback; therefore we estimate it by comparing the deposition rates for 2090s G3BC with the historical period. Jiao et al. (2014) report that the simulated annual mean Arctic (> 60° N) BC deposition for the 2006–2009 period ranges from $13–35 \times 10^7\,\mathrm{kg\,yr^{-1}}$ for the AEROCOM Phase II

ACPD
15, 30043–30079, 2015

models. The annual mean Arctic BC deposition for the 2006–2009 period from our HadGEM2-CCS simulations is 23×10^7 kg yr^{-1}, which is within the AEROCOM range. The annual mean Arctic BC deposition anomaly for the 2090s period in G3BC is 19.6×10^7 kg yr^{-1}. Therefore, the effects of dirty snow in such an SAI scenario would likely be significant, which would have impacts on the distribution of temperature, particularly at high latitudes, potentially confounding some of our conclusions.

This research has highlighted potential climate impacts of injecting various stratospheric aerosols in order to ameliorate global warming. However, further research is needed to further assess the climatic impacts of stratospheric aerosol injection such as the impacts on ozone. Whilst research has shown SAI to be capable of averting certain climate changes such as surface-warming, SAI provides no amelioration for other climate impacts, such as ocean acidification. It is therefore important to note that the safest possible solution to avoiding the sort of climate change instantiated by (e.g.) Fig. 6a of this report is to effectively mitigate greenhouse-gas emissions.

Data sets

Data used to generate figures, graphs, plots and tables are freely available via contacting the lead author: aj247@exeter.ac.uk.

The Supplement related to this article is available online at doi:10.5194/acpd-15-30043-2015-supplement.

Author contributions. A. C. Jones designed the experiments, performed the simulations, analysed the data, and wrote the manuscript with guidance and advice from J. M. Haywood and A. Jones.

Acknowledgements. The authors would like to thank Valentina Aquila for supplying AVHRR and SAGE data, and to Peter Cox, Angus Ferraro, David Keith and Alan Robock for helpful discussions. A. C. Jones was supported by a Met Office/NERC CASE (ref. 580 009 183) PhD

ACPD
15, 30043–30079, 2015

studentship; J. M. Haywood and A. Jones were supported by the Joint UK DECC/Defra Met Office Hadley Centre Climate Programme (GA01101).

References

Aquila, V., Oman, L. D., Stolarski, R. S., Colarco, P. R., and Newman, P. A.: Dispersion of the volcanic sulfate cloud from a Mount Pinatubo–like eruption, J. Geophys. Res., 117, D06216, doi:10.1029/2011JD016968, 2012.

Aquila, V., Garfinkel, C. I., Newman, P. A., Oman, L. D., and Waugh, D. W.: Modifications of the quasi-biennial oscillation by a geoengineering perturbation of the stratospheric aerosol layer, Geophys. Res. Lett., 41, 1738–1744, doi:10.1002/2013GL058818, 2014.

Bala, G., Duffy, P. B., and Taylor, K. E.: Impact of geoengineering schemes on the global hydrological cycle, P. Natl. Acad. Sci. USA, 105, 7664–7669, 2008.

Baldwin, M. P., Gray, L. J., Dunkerton, T. J., Hamilton, K., Haynes, P. H., Randel, W. J., Holton, J. R., Alexander, M. J., Hirota, I., Horinouchi, T., Jones, D. B. A., Kinnersley, J. S., Marquardt, C., Sato, K., and Takahashi, M.: The quasi-biennial oscillation, Rev. Geophys., 39, 179–229, doi:10.1029/1999RG000073, 2001.

Bellouin, N., Rae, J., Johnson, C., Haywood, J., Jones, A., and Boucher, O.: Aerosol forcing in the Hadley Centre CMIP5 simulations by HadGEM2-ES and the role of ammonium nitrate, J. Geophys. Res., 116, D20206, doi:10.1029/2011JD016074, 2011.

Berdahl, M., Robock, A., Ji, D., Moore, J. C., Jones, A., Kravitz, B., and Watanabe, S.: Arctic cryosphere response in the Geoengineering Model Intercomparison Project G3 and G4 scenarios, J. Geophys. Res.-Atmos., 119, 1308–1321, doi:10.1002/2013JD020627, 2014.

Carslaw, K. C. and Kärcher, B.: Stratospheric aerosol processes, in: Assessment of Stratospheric Aerosol Properties, edited by: Thomason, L. and Peter, T., WCRP 124, WMO/TD 1295, SPARC Rep. 4, World Meteorol. Organ., Geneva, Switzerland, 1–152, 2006.

Collins, M., Knutti, R., Arblaster, J., Dufresne, J.-L., Fichefet, T., Friedlingstein, P., Gao, X., Gutowski, W. J., Johns, T., Krinner, G., Shongwe, M., Tebaldi, C., Weaver, A. J., and Wehner, M.: Long-term climate change: projections, commitments and irreversibility, in: Climate Change 2013: The Physical Science Basis, Contribution of Working Group I to the Fifth Assessment Report of the Intergovernmental Panel on Climate Change, edited by: Stocker, T. F., Qin, D., Plattner, G.-K., Tignor, M., Allen, S. K., Boschung, J., Nauels, A.,

ACPD
15, 30043–30079, 2015

Xia, Y., Bex, V., and Midgley, P. M., Cambridge University Press, Cambridge, UK, New York, NY, USA, 1029–1136, 2013.
Crutzen, P.: Albedo enhancement by stratospheric sulfur injections: a contribution to resolve a policy dilemma?, Climatic Change, 77, 211–220, 2006.
d'Almeida, G. A., Koepke, P., and, Shettle, E. P.: Atmospheric Aerosols: Global Climatology and Radiative Characteristics, A. Deepak Publishing, Hampton, USA, 1991.
Dankovic, D., Kuempel, E., Geraci, C., Gilbert, S., Rice, F., Schulte, P., Smith, R., Sofge, C., Wheeler, M., Lentz, T. J., Zumwalde, R., Maynard, A., Attfield, M., Pinheiro, G., Ruder, A., Hubbs, A., Ahlers, H., Lynch, D., Toraason, M., and Vallyathan, V.: Current Intelligence Bulletin 63: Occupational Exposure to Titanium Dioxide, Cincinnati, OH: U.S. Department of Health and Human Services, Public Health Service, Centers for Disease Control and Prevention, National Institute for Occupational Safety and Health, DHHS (NIOSH) Publication No. 2011-160, April 2011, Cincinnati, USA, p. 129, 2011.
Deepak, A. and Gerber, H. E. (Eds.): Report of the Experts Meeting on Aerosols and Their Climatic Effects (Williamsburg, Virginia, March 1983), Rep. WCP-55, World Clim. Programme, World Meteorol. Organ., Geneva, 1983.
Deshler, T. and Anderson-Sprecher, R.: Non-volcanic stratospheric aerosol trends: 1971–2004, in: Assessment of Stratospheric Aerosol Properties, edited by: Thomason, L. and Peter, T., WCRP 124, WMO/TD 1295, SPARC Rep. 4, World Meteorolo. Organ., Geneva, Switzerland, 177–218, 2006.
Driscoll, S., Bozzo, A., Gray, L. J., Robock, A., and Stenchikov, G.: Coupled Model Intercomparison Project 5 (CMIP5) simulations of climate following volcanic eruptions, J. Geophys. Res.-Atmos., 117, D17105, doi:10.1029/2012JD017607, 2012.
English, J. M., Toon, O. B., and Mills, M. J.: Microphysical simulations of sulfur burdens from stratospheric sulfur geoengineering, Atmos. Chem. Phys., 12, 4775–4793, doi:10.5194/acp-12-4775-2012, 2012.
Ferraro, A. J., Highwood, E. J., and Charlton-Perez, A. J.: Stratospheric heating by potential geoengineering aerosols, Geophys. Res. Lett., 38, L24706, doi:10.1029/2011GL049761, 2011.
Ferraro, A. J., Highwood, E. J., and Charlton-Perez, A. J.: Weakened tropical circulation and reduced precipitation in response to geoengineering, Environ. Res. Lett., 9, L24706, doi:10.1029/2011GL049761, 2014.

ACPD
15, 30043–30079, 2015

Forster, P., Ramaswamy, V., Artaxo, P., Berntsen, T., Betts, R., Fahey, D. W., Haywood, J., Lean, J., Lowe, D. C., Myhre, G., Nganga, J., Prinn, R., Raga, G., Schulz, M., and Van Dorland, R.: Changes in atmospheric constituents and in radiative forcing, in: Climate Change 2007: The Physical Science Basis, Contribution of Working Group I to the Fourth Assessment Report of the Intergovernmental Panel on Climate Change, edited by: Solomon, S., Qin, D., Manning, M., Chen, Z., Marquis, M., Averyt, K. B., Tignor, M., and Miller, H. L., Cambridge University Press, Cambridge, UK, New York, NY, USA, 129–234, 2007.

Haywood, J. M., Jones, A., Clarisse, L., Bourassa, A., Barnes, J., Telford, P., Bellouin, N., Boucher, O., Agnew, P., Clerbaux, C., Coheur, P., Degenstein, D., and Braesicke, P.: Observations of the eruption of the Sarychev volcano and simulations using the HadGEM2 climate model, J. Geophys. Res., 115, D21212, doi:10.1029/2010JD014447, 2010.

Haywood, J. M., Jones, A., Bellouin, N., and Stephenson, D.: Asymmetric forcing from stratospheric aerosols impacts Sahelian rainfall, Nat. Clim. Change, 3, 660–665, doi:10.1038/nclimate1857, 2013.

Heckendorn, P., Weisenstein, D., Fueglistaler, S., Luo, B. P., Rozanov, E., Schraner, M., Thomason, L. W., and Peter, T.: The impact of geoengineering aerosols on stratospheric temperature and ozone, Environ. Res. Lett., 4, 045108, doi:10.1088/1748-9326/4/4/045108, 2009.

International Civil Aviation Organisation (ICAO): Manual of the ICAO Standard Atmosphere: Extended to 80 Kilometres (262 200 Feet), Doc 7488/3, 3rd edn., International Civil Aviation Organization, Montreal, Quebec, p. 305, 1993.

Jiao, C., Flanner, M. G., Balkanski, Y., Bauer, S. E., Bellouin, N., Berntsen, T. K., Bian, H., Carslaw, K. S., Chin, M., De Luca, N., Diehl, T., Ghan, S. J., Iversen, T., Kirkevåg, A., Koch, D., Liu, X., Mann, G. W., Penner, J. E., Pitari, G., Schulz, M., Seland, Ø., Skeie, R. B., Steenrod, S. D., Stier, P., Takemura, T., Tsigaridis, K., van Noije, T., Yun, Y., and Zhang, K.: An AeroCom assessment of black carbon in Arctic snow and sea ice, Atmos. Chem. Phys., 14, 2399–2417, doi:10.5194/acp-14-2399-2014, 2014.

Kawatani, Y. and Hamilton, K.: Weakened stratospheric quasibiennial oscillation driven by increased tropical mean upwelling, Nature, 497, 478–481, doi:10.1038/nature12140, 2013.

Kharin, V. V., Zwiers, F. W., Zhang, X., and Wehner, M.: Changes in temperature and precipitation extremes in the CMIP5 ensemble, Climatic Change, 119, 345–357, doi:10.1007/s10584-013-0705-8, 2013.

ACPD
15, 30043–30079, 2015

Kravitz, B., Robock, A., Boucher, O., Schmidt, H., Taylor, K. E., Stenchikov, G., and Schulz, M.: The Geoengineering Model Intercomparison Project (GeoMIP), Atmos. Sci. Lett., 12, 162–167, doi:10.1002/asl.316, 2011.

Kravitz, B., Robock, A., Shindell, D. T., and Miller, M. A.: Sensitivity of stratospheric geoengineering with black carbon to aerosol size and altitude of injection, J. Geophys. Res., 117, D09203, doi:10.1029/2011JD017341, 2012.

Kravitz, B., Robock, A., Forster, P. M., Haywood, J. M., Lawrence, M. G., and Schmidt, H.: An overview of the Geoengineering Model Intercomparison Project (GeoMIP), J. Geophys. Res.-Atmos., 118, 13,103–13,107, doi:10.1002/2013JD020569, 2013.

Lombardo, K., Colle, B. A., and Zhang, Z.: Evaluation of historical and future cool season precipitation over the eastern United States and western Atlantic storm track using CMIP5 models, J. Climate, 28, 451–467, doi:10.1175/JCLI-D-14-00343.1, 2015.

Marks, A. A. and King, M. D.: The effect of snow/sea ice type on the response of albedo and light penetration depth (*e*-folding depth) to increasing black carbon, The Cryosphere, 8, 1625–1638, doi:10.5194/tc-8-1625-2014, 2014.

Meinshausen, M., Smith, S. J., Calvin, K. V., Daniel, J. S., Kainuma, M. L. T., Lamarque, J.-F., Matsumoto, K., Montzka, S. A., Raper, S. C. B., Riahi, K., Thomson, A. M., Velders, G. J. M., and Van Vuuren, D.: "The RCP Greenhouse Gas Concentrations and their Extension from 1765 to 2300," Climatic Change, 109, 213–241, doi:10.1007/s10584-011-0156-z, 2011.

Niemeier, U., Schmidt, H., and Timmreck, C.: The dependency of geoengineered sulfate aerosol on the emission strategy, Atmos. Sci. Lett., 12, 189–194, doi:10.1002/asl.304, 2011.

Oman, L., Robock, A., Stenchikov, G. L., and Thordarson, T.: High-latitude eruptions cast shadow over the African monsoon and the flow of the Nile., Geophys. Res. Lett., 33, L1871116, doi:10.1029/2006GL027665, 2006.

Pierce, J. R., Weisenstein, D. K., Heckendorn, P., Peter, T., and Keith, D. W.: Efficient formation of stratospheric aerosol for climate engineering by emission of condensible vapor from aircraft, Geophys. Res. Lett., 37, L18805, doi:10.1029/2010GL043975, 2010.

Pitari, G., Aquila, V., Kravitz, B., Robock, A., Watanabe, S., Cionni, I., De Luca, N., Di Genova, G., Mancini, E., and Tilmes, S.: Stratospheric ozone response to sulfate geoengineering: results from the Geoengineering Model Intercomparison Project (GeoMIP), J. Geophys. Res.-Atmos., 119, 2629–2653, doi:10.1002/2013JD020566, 2014.

ACPD
15, 30043–30079, 2015

Pope, F. D., Braesicke, P., Grainger, R. G., Kalberer, M., Watson, I. M., Davidson, P. J., and Cox, R. A.: Stratospheric aerosol particles and solar-radiation management, Nat. Clim. Change, 2, 713–719, doi:10.1038/nclimate1528, 2012.

Pruppacher, H. R. and Klett, J. D.: Microphysics of Clouds and Precipitation, D. Reidel Publishing Company, Dordretch, Holland, ISBN: 978-90-277-1106-9, Reprinted 1980.

Ramaswamy, V., Boucher, O., Haigh, J., Hauglustaine, D., Haywood, J., Myhre, G., Nakajima, T., Shi, G. Y., and Solomon, S.: Radiative forcing of climate change, in: Climate Change 2001: The Scientific Basis, Contribution of Working Group I to the Third Assessment Report of the Intergovernmental Panel on Climate Change, edited by: Houghton, J. T., Ding, Y., Griggs, D. J., Noguer, M., van der Linden, P. J., Dai, X., Maskell, K., and Johnson, C. A., Cambridge University Press, Cambridge, UK, New York, NY, USA, 349–416, 2001.

Rasch, P. J., Tilmes, S., Turco, R. P., Robock, A., Oman, L., Chen, C.-C., Stenchikov, G. L., and Garcia, R. R.: An overview of geoengineering of climate using stratospheric sulphate aerosols, Philos. T. R. Soc. A, 366, 4007–4037, doi:10.1098/rsta.2008.0131, 2008.

Ribarsky, M. W.: Titanium dioxide, in: Handbook of Optical Constants of Solids, edited by: Palik, E., Academic, Orlando, Fl., 795–804, 1985.

Robock, A., Oman, L., and Stenchikov, G. L.: Regional climate responses to geoengineering with tropical and Arctic SO_2 injections, J. Geophys. Res., 113, D16101, doi:10.1029/2008JD010050, 2008.

Schoeberl, M. R., Douglass, A. R., Stolarski, R. S., Pawson, S., Strahan, S. E., and Read, W.: Comparison of lower stratospheric tropical mean vertical velocities, J. Geophys. Res., 113, D24109, doi:10.1029/2008JD010221, 2008.

Shepherd, J., Caldeira, K., Cox, P., Haigh, J., Keith, D., Launder, B., Mace, G., MacKerron, G., Pyle, J., Rayer, S., Redgwell, C., and Watson, A.: Geoengineering the Climate: Science, Governance, and Uncertainty, Royal Society Policy document 10/09, ISBN: 978-0-85403-773-5, The Royal Society, London, UK, p. 82, 2009.

Stenchikov, G., Robock, A., Ramaswamy, V., Schwarzkopf, M. D., Hamilton, K., and Ramachandran, S.: Arctic oscillation response to the 1991 Mount Pinatubo eruption: effects of volcanic aerosols and ozone depletion, J. Geophys. Res., 107, 4803, doi:10.1029/2002JD002090, 2002.

Taylor, K. E., Stouffer, R. J., and Meehl, G. A.: An overview of CMIP5 and the experiment design, B. Am. Meteorol. Soc., 93, 485–498, doi:10.1175/BAMS-D-11-00094.1, 2012.

ACPD
15, 30043–30079, 2015

Tegtmeier, S., Kruger, K., Wohltmann, I., Schoellhammer, K., and Rex, M.: Variations of the residual circulation in the Northern Hemispheric winter, J. Geophys. Res., 113, D16109, doi:10.1029/2007JD009518, 2008.

Teller, E., Wood, L., and Hyde, R.: Global Warming and Ice Ages: I. Prospects for Physics-Based Modulation of Global Change, Lawrence Livermore National Laboratory Publication, 22nd International Seminar on Planetary Emergencies, Erice (Sicily), Italy, 20–23 August 1997, in preparation, UCRL-JC-128715, 18 pp., 1997.

The HadGEM2 Development Team: G. M. Martin, Bellouin, N., Collins, W. J., Culverwell, I. D., Halloran, P. R., Hardiman, S. C., Hinton, T. J., Jones, C. D., McDonald, R. E., McLaren, A. J., O'Connor, F. M., Roberts, M. J., Rodriguez, J. M., Woodward, S., Best, M. J., Brooks, M. E., Brown, A. R., Butchart, N., Dearden, C., Derbyshire, S. H., Dharssi, I., Doutriaux-Boucher, M., Edwards, J. M., Falloon, P. D., Gedney, N., Gray, L. J., Hewitt, H. T., Hobson, M., Huddleston, M. R., Hughes, J., Ineson, S., Ingram, W. J., James, P. M., Johns, T. C., Johnson, C. E., Jones, A., Jones, C. P., Joshi, M. M., Keen, A. B., Liddicoat, S., Lock, A. P., Maidens, A. V., Manners, J. C., Milton, S. F., Rae, J. G. L., Ridley, J. K., Sellar, A., Senior, C. A., Totterdell, I. J., Verhoef, A., Vidale, P. L., and Wiltshire, A.: The HadGEM2 family of Met Office Unified Model climate configurations, Geosci. Model Dev., 4, 723–757, doi:10.5194/gmd-4-723-2011, 2011.

Tilmes, S., Garcia, R. R., Kinnison, D. E., Gettelman, A., and Rasch, P. J.: Impact of geo-engineered aerosols on the troposphere and stratosphere, J. Geophys. Res., 114, D12305, doi:10.1029/2008JD011420, 2009.

Tilmes, S., Kinnison, D. E., Garcia, R. R., Salawitch, R., Canty, T., Lee-Taylor, J., Madronich, S., and Chance, K.: Impact of very short-lived halogens on stratospheric ozone abundance and UV radiation in a geo-engineered atmosphere, Atmos. Chem. Phys., 12, 10945–10955, doi:10.5194/acp-12-10945-2012, 2012.

Tilmes, S., Fasullo, J., Lamarque, J.-F., Marsh, D. R., Mills, M., Alterskjær, K., Muri, H., Kristjánsson, J. E., Boucher, O., Schulz, M., Cole, J. N. S., Curry, C. L., Jones, A., Haywood, J., Irvine, P. J., Ji, D., Moore, J. C., Karam, D. B., Kravitz, B., Rasch, P. J., Singh, C., Yoon, J.-H., Niemeier, U., Schmidt, H., Robock, A., Yang, S., and Watanabe, S.: The hydrological impact of geoengineering in the Geoengineering Model Intercomparison Project (GeoMIP), J. Geophys. Res.-Atmos., 118, 11036–11058, doi:10.1002/jgrd.50868, 2013.

ACPD
15, 30043–30079, 2015

Weisenstein, D. K. and Keith, D. W.: Solar geoengineering using solid aerosol in the stratosphere, Atmos. Chem. Phys. Discuss., 15, 11799–11851, doi:10.5194/acpd-15-11799-2015, 2015.

Yang, H., Zhu, S., and Pan, N.: Studying the mechanisms of titanium dioxide as ultraviolet-blocking additive for films and fabrics by an improved scheme, J. Appl. Polym. Sci., 92, 3201–3210, 2004.

Yu, X., Moore, J. C., Cui, X., Rinke, A., Ji, D., Kravitz, B., and Yoon, J.-H.: Impacts, effectiveness and regional inequalities of the GeoMIP G1 to G4 solar radiation management scenarios, Global Planet. Change, 129, 10–22, doi:10.1016/j.gloplacha.2015.02.010, 2015.

ACPD
15, 30043–30079, 2015

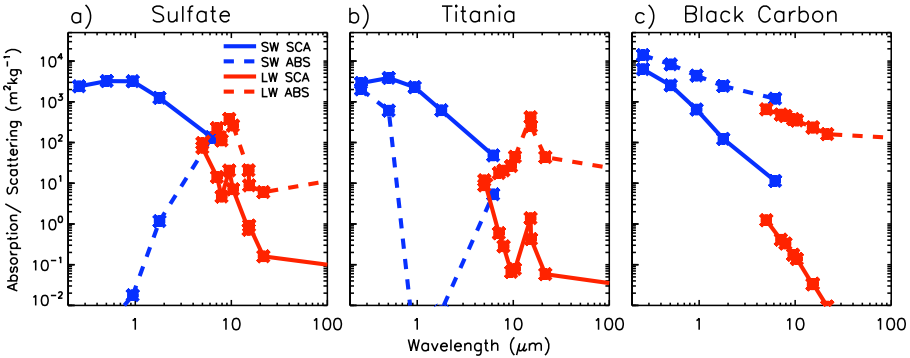

Figure 1. Optical properties as a function of wavelength for **(a)** accumulation-mode sulfate, **(b)** titania, **(c)** black carbon.

ACPD
15, 30043–30079, 2015

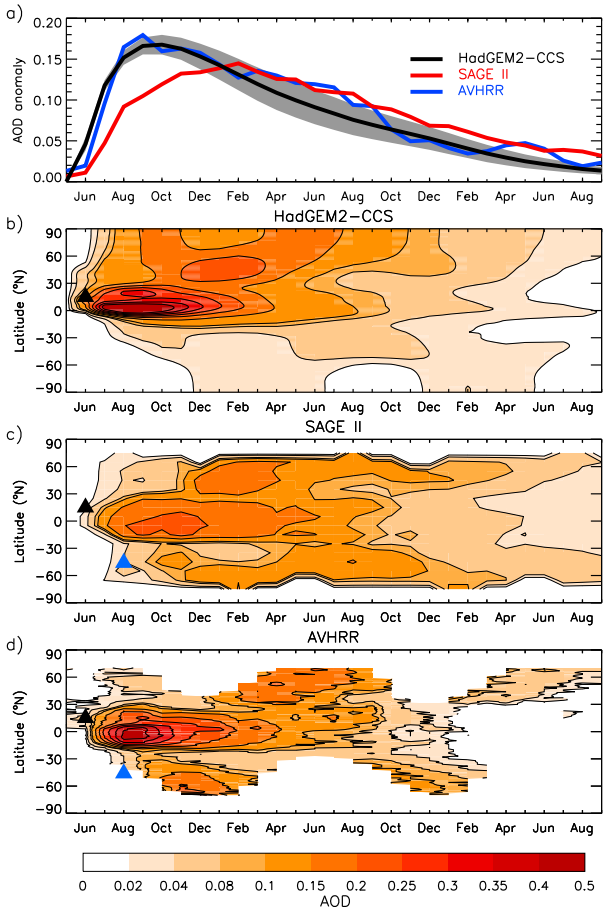

Figure 2. (a) 75° S–75° N-mean 550 nm sulfate AOD anomaly for the Pinatubo simulations and observations, **(b–d)** timeseries of zonal-mean 550 nm sulfate AOD anomaly.

ACPD
15, 30043–30079, 2015

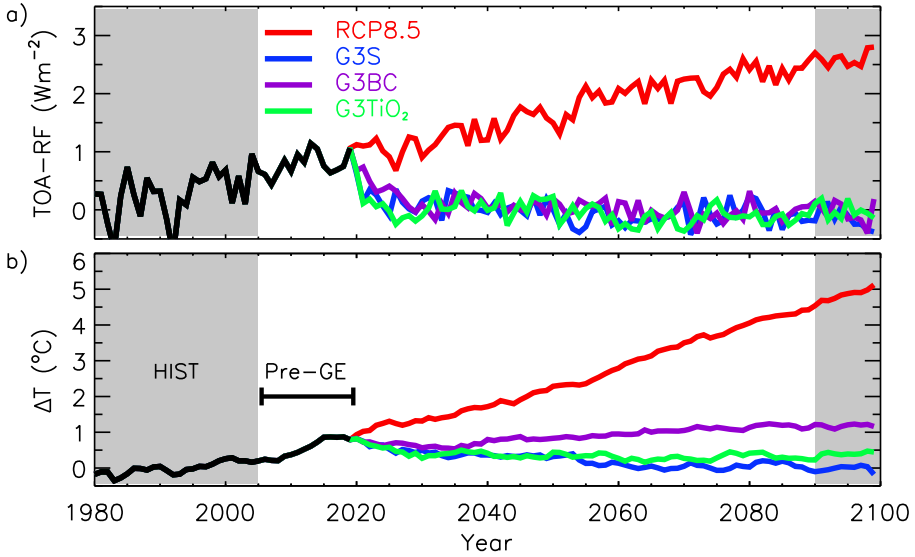

Figure 3. Timeseries of annual/global-mean **(a)** top-of-the-atmosphere radiative flux anomaly with respect to the pre-industrial control simulation **(b)** near-surface air temperature anomaly with respect to the HIST period.

ACPD
15, 30043–30079, 2015

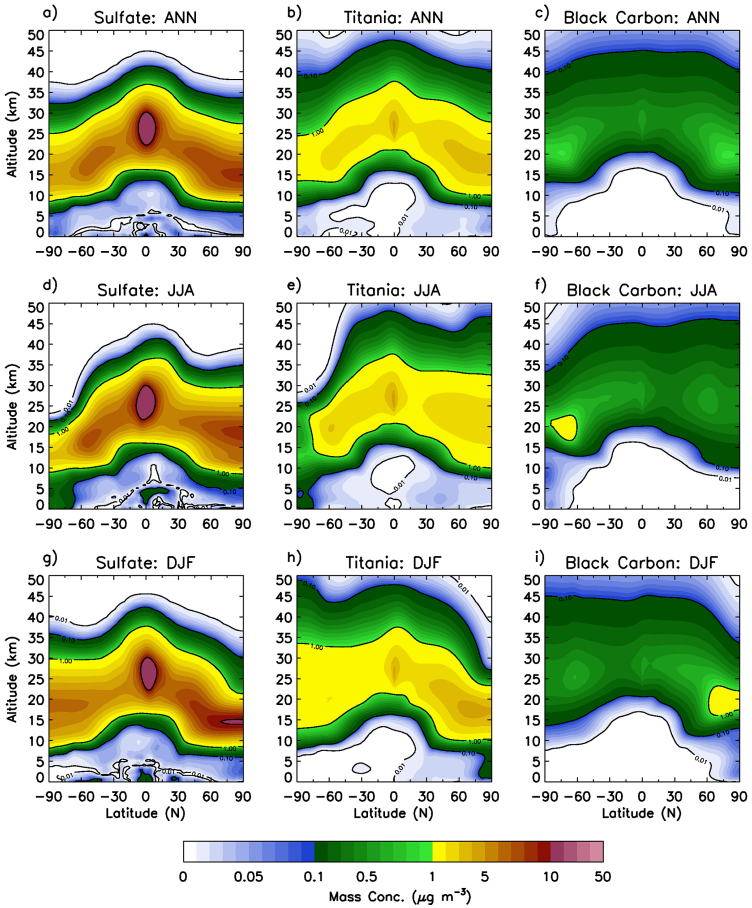

Figure 4. Annual and seasonal zonal-mean mass concentration anomalies for sulfate (G3S – left), titania ($G3TiO_2$ – centre) and black carbon (G3BC – right).

ACPD
15, 30043–30079, 2015

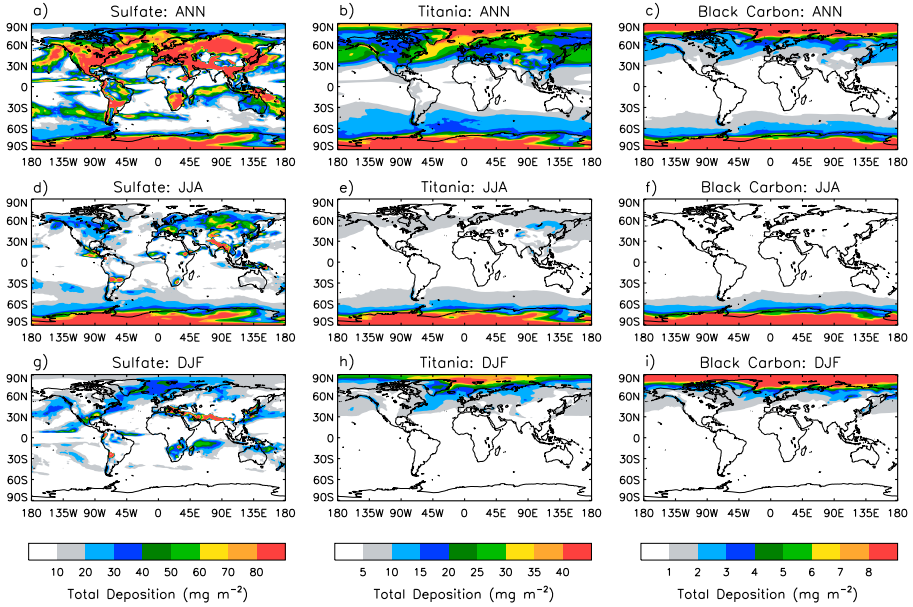

Figure 5. Annual and seasonal total deposition anomalies (in units of mg m^{-2} yr^{-1} and 0.25× mg m^{-2} yr^{-1} respectively).

ACPD
15, 30043–30079, 2015

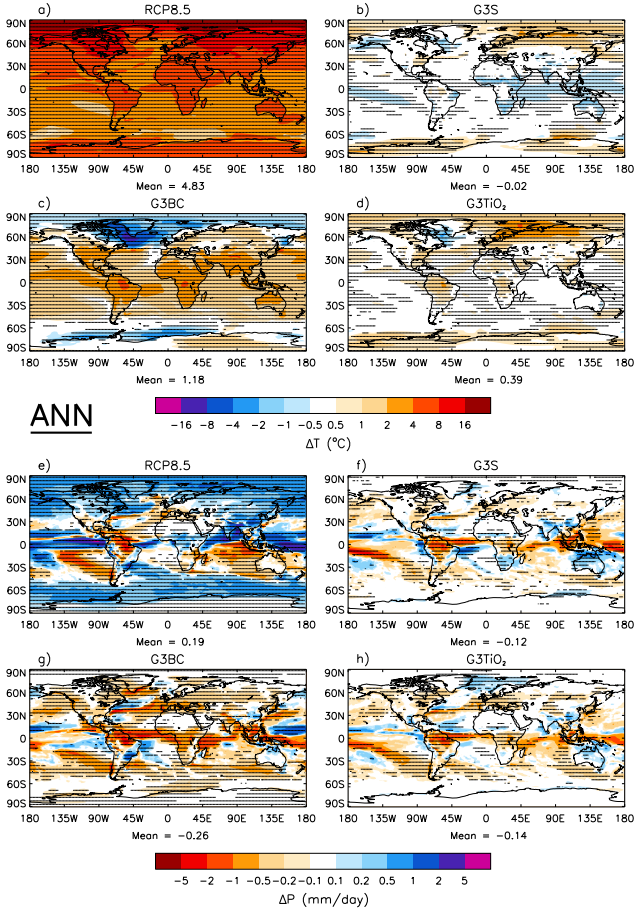

Figure 6. Annual-mean near-surface air temperature (top) and precipitation rate (bottom) anomalies with respect to HIST. Stipling indicates where changes are significant at the 5 % level using a two-tailed Student's *t* test.

ACPD
15, 30043–30079, 2015

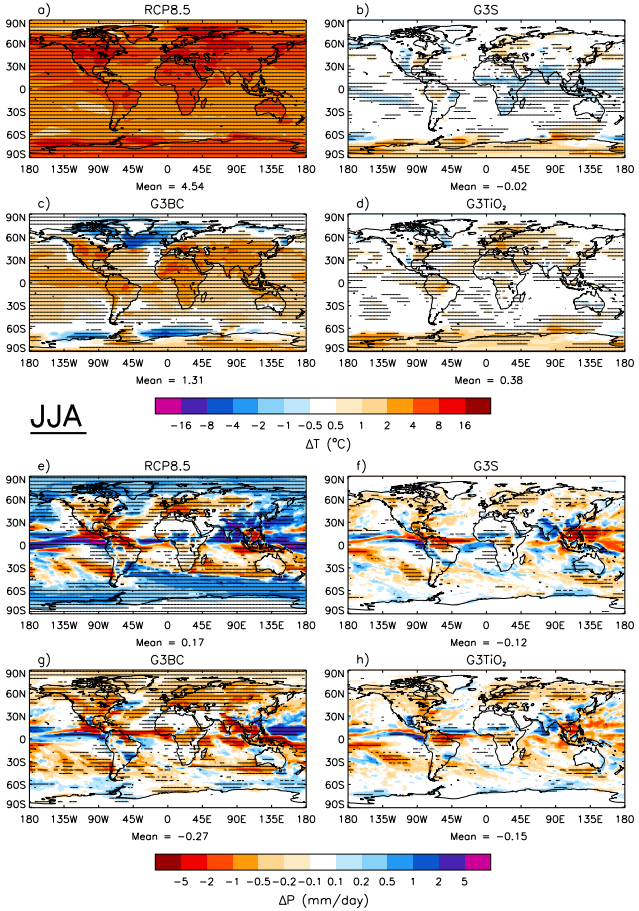

Figure 7. JJA near-surface air temperature (top) and precipitation rate (bottom) anomalies with respect to HIST.

ACPD
15, 30043–30079, 2015

Climatic impacts of stratospheric geoengineering with sulfate, black carbon and titania injection

A. C. Jones et al.

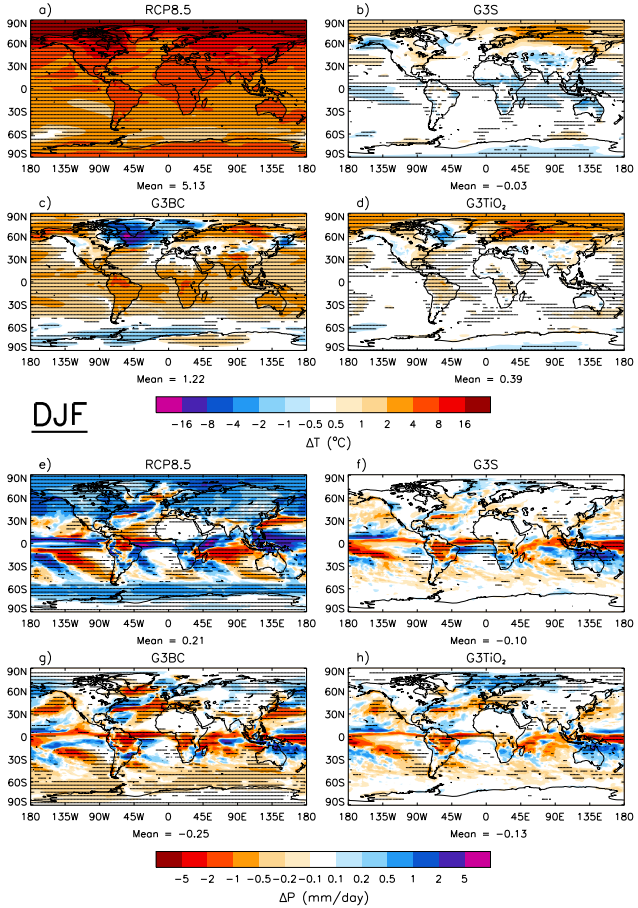

Figure 8. DJF near-surface air temperature (top) and precipitation rate (bottom) anomalies with respect to HIST.

ACPD
15, 30043–30079, 2015

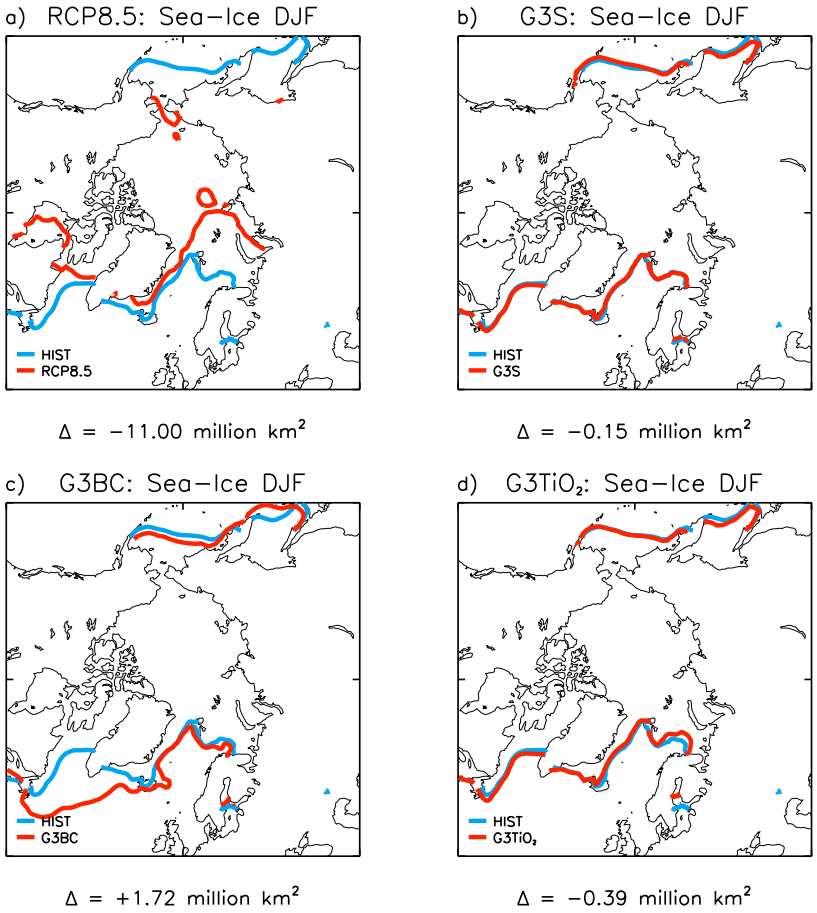

Figure 9. DJF Northern Hemisphere sea-ice edge plotted with the HIST extent.

ACPD
15, 30043–30079, 2015

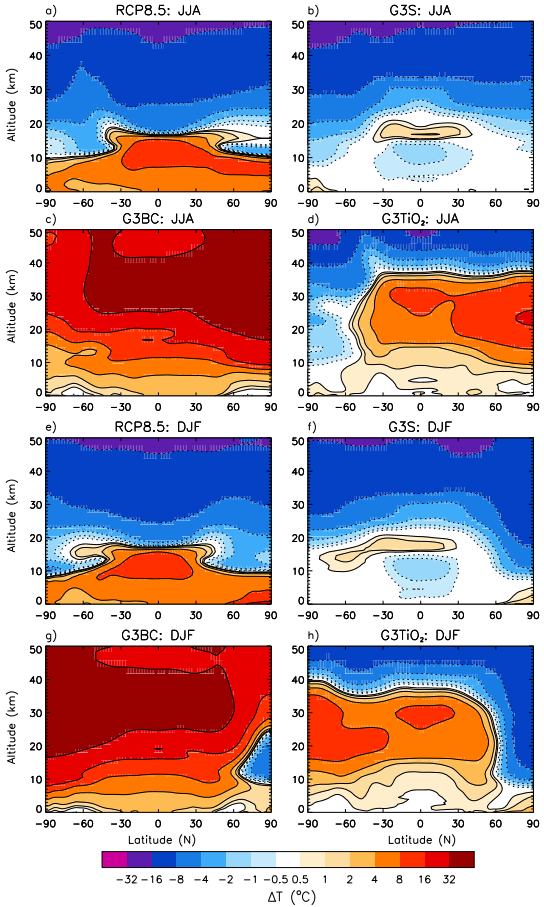

Figure 10. JJA (top) and DJF (bottom) zonal-mean temperature anomaly with altitude, with respect to HIST.

ACPD
15, 30043–30079, 2015

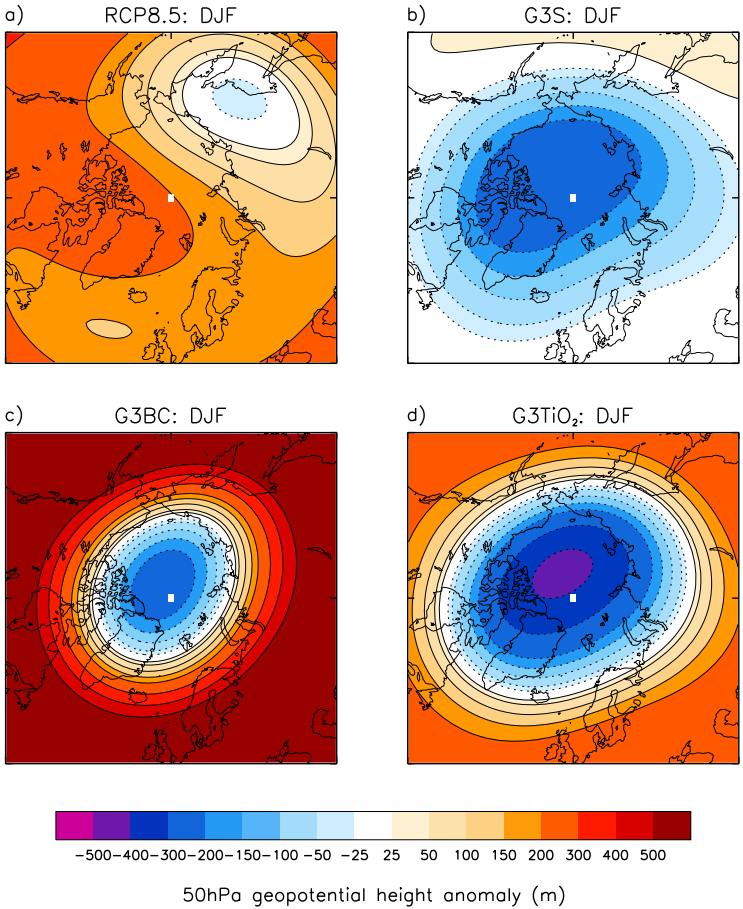

Figure 11. DJF 50 hPa geopotential height anomaly.

ACPD
15, 30043–30079, 2015

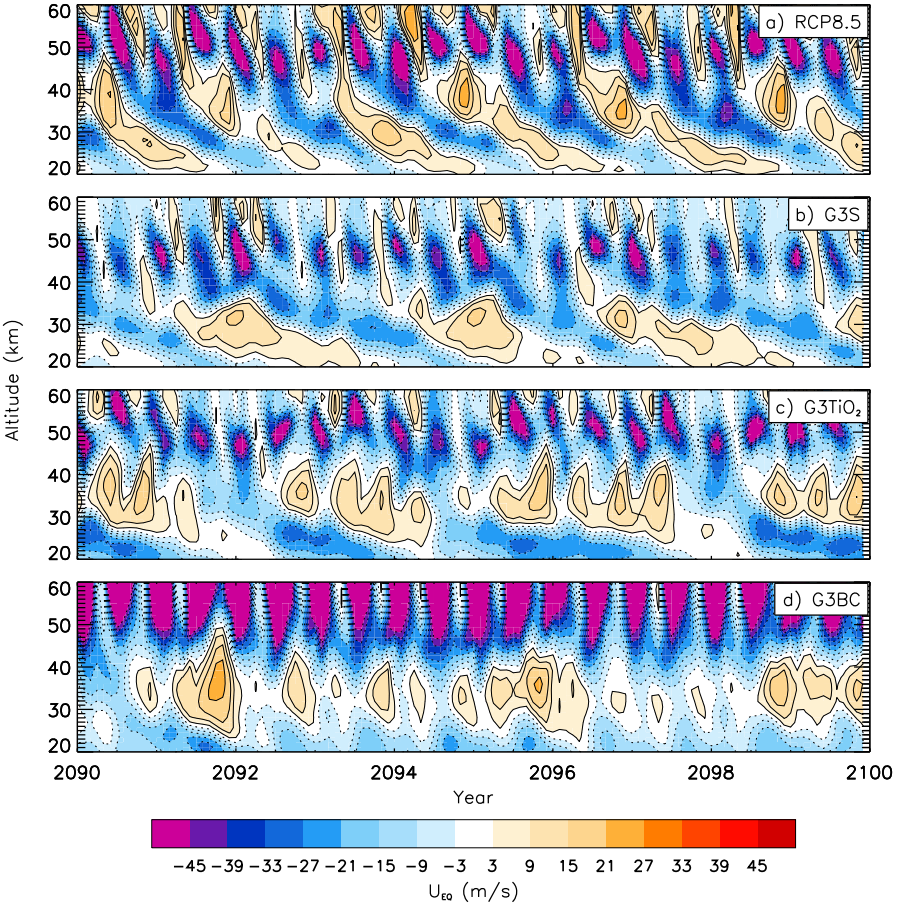

Figure 12. Timeseries of equatorial (5° S–5° N) zonal-mean zonal wind profile.

ACPD
15, 30043–30079, 2015

Climatic impacts of stratospheric geoengineering with sulfate, black carbon and titania injection

A. C. Jones et al.